ACS OMEGA

http://pubs.acs.org/journal/acsodf

Article

Highly Efficient Removal for Methylene Blue and Cu^{2+} onto UiO-66 Metal–Organic Framework/Carboxylated Graphene Oxide-Incorporated Sodium Alginate Beads

Abdelazeem S. Eltaweil,* Injy M. Mamdouh, Eman M. Abd El-Monaem, and Gehan M. El-Subruiti

Cite This: *ACS Omega* 2021, 6, 23528–23541

Read Online

ACCESS | Metrics & More | Article Recommendations | Supporting Information

ABSTRACT: Herein, we report a new metal–organic framework (MOF)-based composite beads adsorbent made via incorporating UiO-66 MOF, carboxylated graphene oxide (GOCOOH) into sodium alginate for efficient removal of methylene blue dye, and Cu^{2+} ions. The successful fabrication of the synthesized UiO-66/GOCOOH@SA composite beads was confirmed by means of X-ray diffraction, Fourier transform infrared, scanning electron microscopy, zeta potential, X-ray photoelectron spectroscopy analysis, and thermogravimetric analysis and BET measurement. The incorporation of both UiO-66 and GOCOOH into SA beads greatly increased their adsorption efficiency for the removal of both MB and Cu^{2+} with maximum adsorption capacities of 490.72 and 343.49 mg/g, respectively. The removal process of both MB and Cu^{2+} follows the pseudo-second-order model and Freundlich isotherm model. A plausible adsorption mechanism was discussed in detail. Regeneration tests clarified that the removal efficiencies toward both MB and Cu^{2+} remained higher than 87% after five cycles. These results reveal the potentiality of UiO-66/GOCOOH@SA beads as an excellent adsorbent.

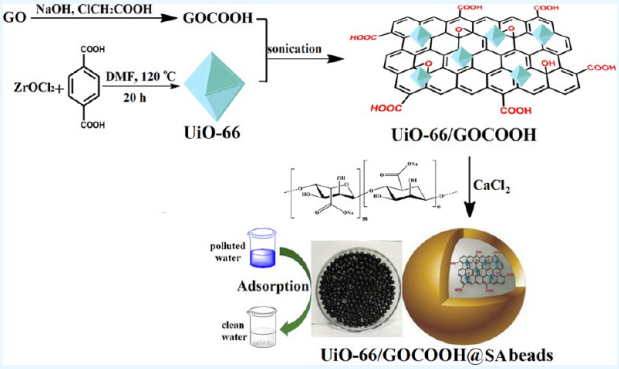

1. INTRODUCTION

Undoubtedly, water is one of nature's precious gifts to mankind that should be protected instead of being contaminated with dangerous substances. So, if we do not assess the vast disaster that we are facing, which is "water pollution", then our life on the planet will become under threat. Notably, synthetic dyes are considered the most hazardous sort of contaminants that pose jeopardy to human health as well as marine life.[1−5] Among these assorted dyes, cationic methylene blue (MB) has a planar structure, rendering it highly soluble in water.[6,7] As a result, it may damage marine life since sunlight is prevented to penetrate into water bodies and reoxygenation of the marine system is interrupted.[8] In addition, there is a severe impact on human health such as methemoglobinemia, convulsions, nausea, eye burning, tachycardia, cyanosis, etc.[9] Despite the mentioned risks of MB, potential industries mainly build upon it, including food, printing, medicine, coloring food, cotton, and wood.[10] Moreover, heavy metals are another case in point of hazard contaminants; however, their importance in several industries includes fertilizers, paints, pigments, etc.[11,12] Discharge of the cationic metal ions such as copper (Cu^{2+}) into water resources uncertainly aggravates fatal diseases such as anemia, nausea, stomach intestinal distress, cyanosis, kidney damage, and rapid respiration that may eventually lead to coma and even death.[13] Accordingly, physicochemical techniques have been developed to get rid of this enormous risk such as flocculation,[14] ultrafiltration,[15] advanced oxidation,[16] photocatalysis,[17−21] catalysis,[22,23] biological treatment,[24] and adsorption.[25−28] Due to the simplicity, high efficiency, and low cost of the adsorption technique, it has been considered the best choice for the removal of contaminants from water bodies.[29−32]

Sodium alginate (SA) is an anionic polysaccharide that is extracted from brown seaweed.[33] SA is a well-known polysaccharide consisting of two monomers, α-L-guluronic acid (G units) and β-D-mannuronic acid (M units), linked together by a β-1,4-glycosidic bond. SA is an environmentally friendly biopolymer because of its biodegradability and nontoxic nature.[34,35] Based on these criteria, SA has drawn special attention in wastewater treatment applications as a premium encapsulating material owing to its notable advantages including strong gelation, high chemical stability, and biocompatibility.[36,37] In addition, the backbone chain of

Received: July 7, 2021
Published: September 3, 2021

https://doi.org/10.1021/acsomega.1c03479
ACS Omega 2021, 6, 23528–23541

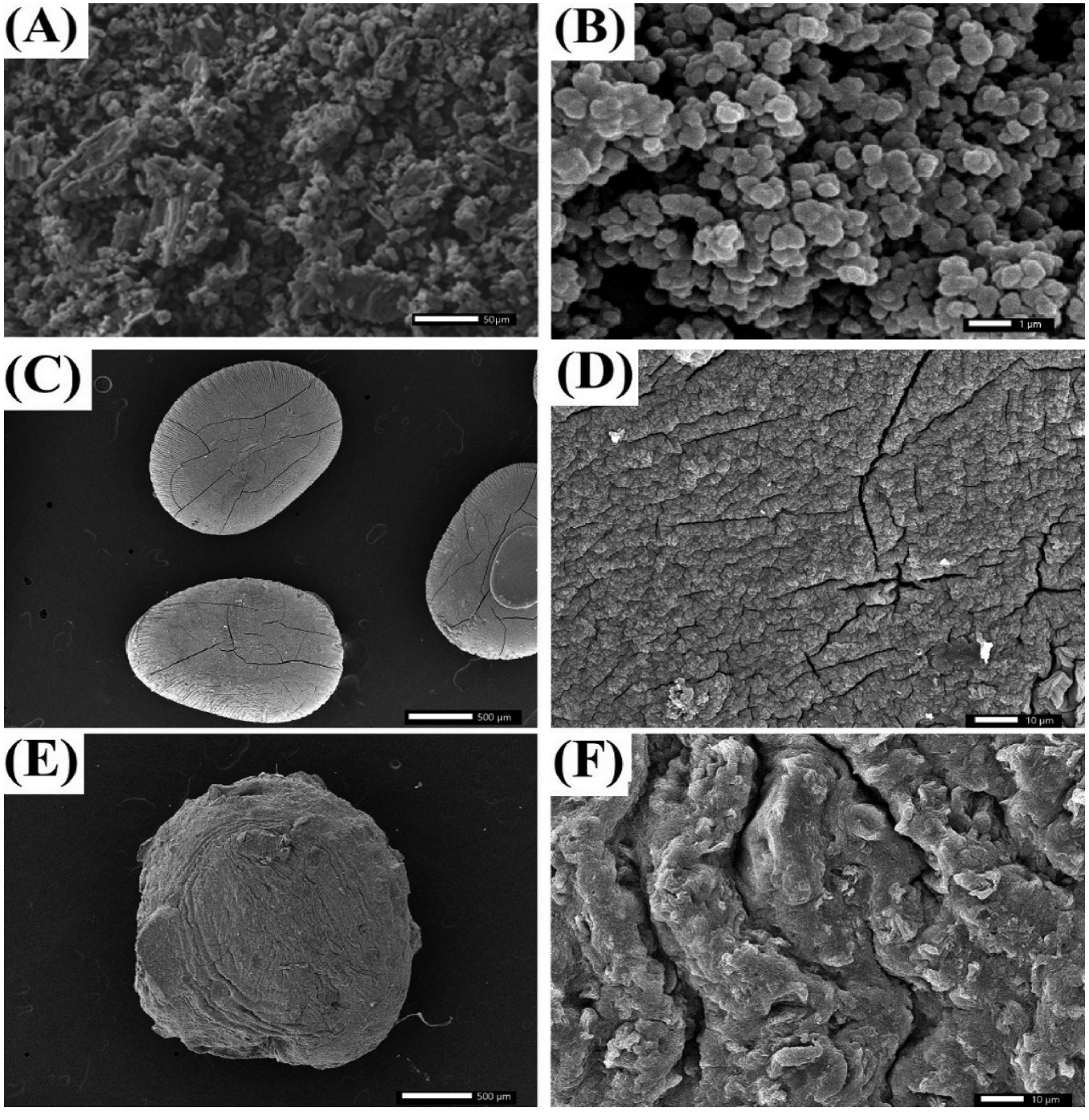

Figure 1. SEM images of (A) GOCOOH, (B) UiO-66, (C, D) SA beads, and (E, F) UiO-66/GOCOOH@SA composite beads.

SA possesses plentiful functional groups such as hydroxyl and carboxyl groups that reinforce the chelating ability toward the cationic pollutants whether in heavy metals or dyes.[38] However, the adsorption capacity and the mechanical properties of SA need improvements to utilize it efficiently in the field of wastewater treatment.

Metal−organic frameworks (MOFs) represent a new category of porous materials with ordered network structures building up from organic−inorganic hybrids.[25] MOFs have acquired tremendous attention in diverse fields including gas storage, photobased reactions, adsorption, membranes, and drug delivery.[39−41] UiO-66 MOF and its derivatives have been extensively utilized in adsorption owing to their excellent water stability and high adsorption capacities.[42−44]

It has been reported that graphene oxide (GO) contains a variety of functional groups including C−O−C (epoxy) groups, −OH (hydroxyl) groups, and edged −COOH (carboxylic) groups. These varieties of functional groups make GO one of the extensively utilized materials to create new pores and new active sites in adsorbent composites.[45,46] The combination between high surface area MOFs, GO derivatives, and biopolymers could greatly enhance their properties as well as avoid their disadvantages.[47] Moreover, the encapsulation of powder adsorbents into biopolymer beads

https://doi.org/10.1021/acsomega.1c03479
ACS Omega 2021, 6, 23528−23541

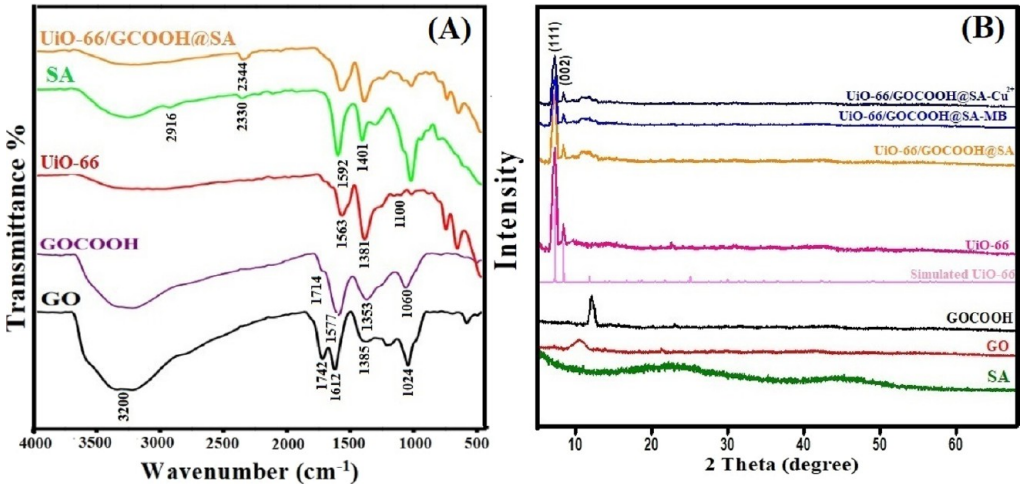

Figure 2. (A) FTIR spectra of GO, GOCOOH, UiO-66, SA, and UiO-66/GOCOOH@SA composite beads; (B) XRD patterns of SA, GO, GOCOOH, UiO-66, UiO-66/GOCOOH@SA composite beads, UiO-66/GOCOOH@SA composite beads after adsorption of MB and Cu^{2+}.

such as SA is one of the most felicitous ways to provide highly efficient, easily regenerable, and reusable adsorbents.[48,49]

Actually, there are previous studies that reported the modification of UiO-66 with GO and its derivatives at which GO provides more active sites, enhancing the adsorbability of UiO-66. Nevertheless, the efficient UiO-66/GO composites in their powder form suffer from low reusability and difficult separation. So, incorportation of UiO-66/GO composites into a host like SA is an effective solution to overcome this flaw. Accordingly, we aimed to fabricate a devoloped adsorbent taking into consideration both efficacy and reusability criteria. The developed UiO-66/GOCOOH@SA composite beads were fabricated for the adsorptive removal of the noxious cationic contaminants (MB dye and Cu^{2+} ions) since the matrix of the fabricated beads has abundant anionic functional groups, suggesting a strong electrostatic interaction between the fabricated beads and both MB dye and Cu^{2+} ions. To the best of our knowledge, there is no reported work on the removal of Cu^{2+} onto MOF/GO derivatives. Furthermore, the high capability of SA to chelate the MB dye and Cu^{2+} ions is via the ion-exchange mechanism. Hence, our study focused on (i) fabricating an efficient adsorbent that has high recyclability and reusability many times, attained by the supporting host SA that provides easy and perfect separtion, (ii) characterizing the fabricated UiO-66/GOCOOH@SA composite beads using SEM, FTIR, XRD, XPS, TGA, BET, and zeta potential, (iii) evaluating the adsorption capacity of UiO-66/GOCOOH@SA composite beads in the removal of both MB dye and Cu^{2+} ions from wastewater, and (iv) exploring the adsorption mechanism based on XPS analysis.

2. RESULTS AND DISCUSSION

2.1. Characterization of UiO-66/GOCOOH@SA Composite Beads. *2.1.1. SEM.* The SEM image of GOCOOH (Figure 1A) shows crushed sheets, suggesting that the sheets of GO were destroyed during the carboxylation step.[25] The SEM image for UiO-66 (Figure 1B) shows the quasi-spherical morphology of UiO-66 particles that may be caused by the rapid nucleation of MOF particles during the solvothermal process. SEM image for SA beads (Figure 1C) shows the elongated shape of the dry SA beads. In addition, Figure 1E reveals that the surface of SA beads is quite coarse with large cracks, resulting from the collapse of SA layers during dehydration, which may be attributed to the low mechanical strength.[50] However, the SEM images of the dry UiO-66/GOCOOH@SA composite beads (Figure 1E,F) manifest a spherical shape of the fabricated beads with a size of around 2−3 mm. The surface of the fabricated spherical beads is highly rugged owing to the variation in the chemical composition of their components. Furthermore, it is obvious that no cracks appeared on the surface of UiO-66/GOCOOH@SA composite beads, suggesting that the composite beads possess enhanced mechanical strength compared to SA beads.

2.1.2. FTIR. Figure 2A illustrates the FTIR spectra of GO, GOCOOH, UiO-66, SA, and UiO-66/GOCOOH@SA composite beads. It is apparent that all FTIR spectra show a broad band at around 3200 cm^{-1}, which belongs to OH stretching vibrations of adsorbed water. The FTIR spectrum of GO points out the distinguishing bands at 1045, 1385, 1612, and 1724 cm^{-1}, which are related to the epoxy C−O, C−OH, C═C, and C═O stretching, respectively.[51,52] For GOCOOH, the FTIR spectrum reveals two bands at 1060 and 1714 cm^{-1}, which are ascribed to the C−H stretching vibration and C═O stretching, respectively. Moreover, bands at 1577 and 1353 cm^{-1} are assigned to the symmetric and asymmetric COOH vibration, respectively.[53] The UiO-66 spectrum exhibits bands at 453 and 737 cm^{-1}, which are attributed to the C−H vibration, whereas the band at 665 cm^{-1} is ascribed to the C═C stretching vibration of the aromatic ring of H_2BDC. In addition, sharp peaks at 1563 and 1381 cm^{-1} are assigned to the asymmetric and symmetric COO^- group stretching vibration, respectively. The successful fabrication of UiO-66 was assured by the manifestation of the distinctive peak at 1100 cm^{-1}, which belongs to the Zr−O bond, asserting the formation of the coordination bond between Zr and H_2BDC.[42] For SA, the spectrum exhibits bands at 799 and 1019 cm^{-1} that are attributed to the C−H bending and C−O stretching, respectively. Two bands at 1592 and 1401 cm^{-1} are related to symmetric and asymmetric COO^- group stretching, respectively. In addition, the band at 2916 cm^{-1} is assigned to the C−H stretching vibration, while the band observed at 2330 cm^{-1} is ascribed to the CO_2 group.[54] The FTIR of UiO-66/GOCOOH@SA composite beads clarifies the main distinctive peaks of GOCOOH, UiO-66, and SA with a decrease in the peak intensity. In addition, an obvious shift in the CO_2 peak

https://doi.org/10.1021/acsomega.1c03479
ACS Omega 2021, 6, 23528−23541

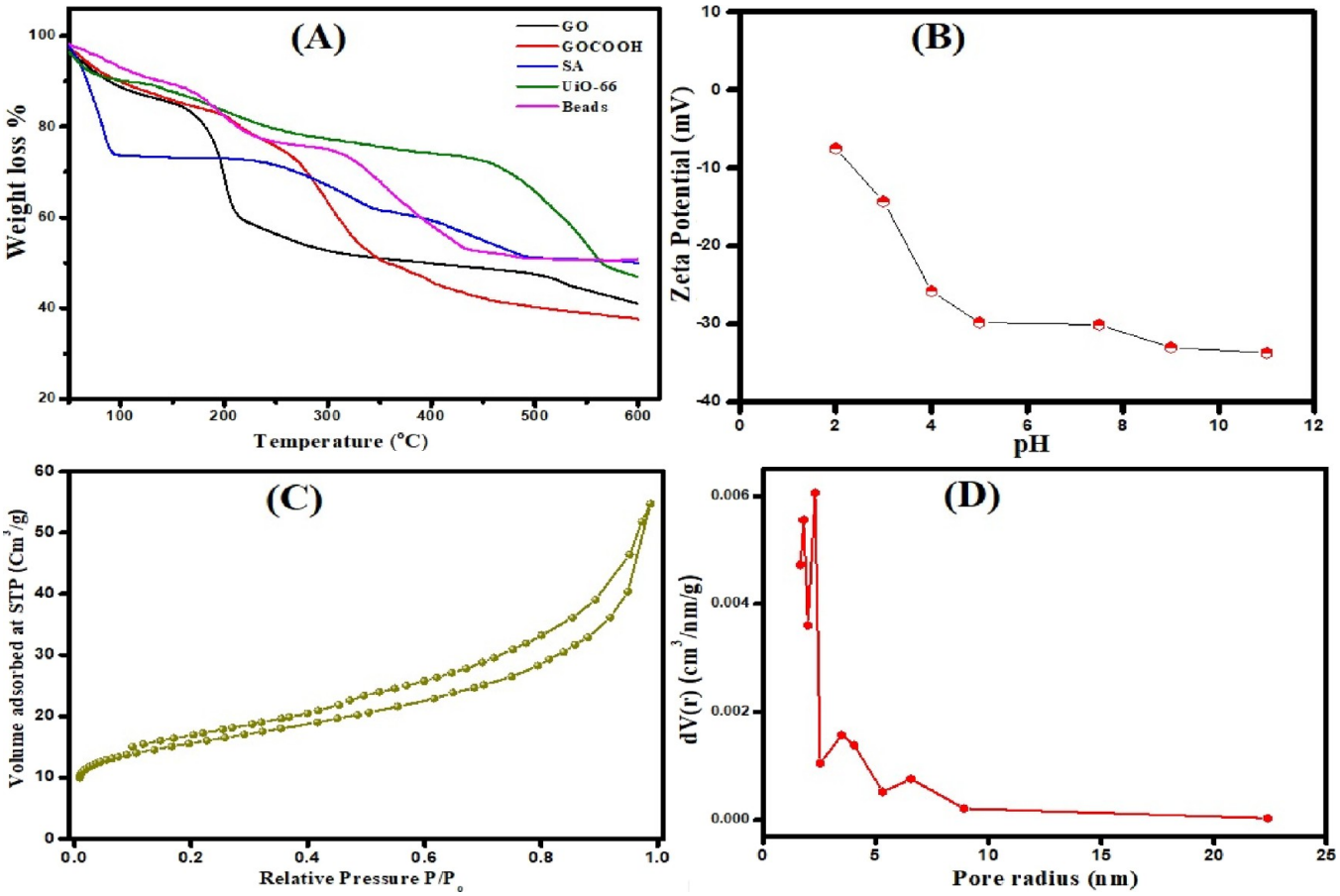

Figure 3. (A) TGA curves of GO, GOCOOH, SA, UiO-66, and UiO-66/GOCOOH@SA composite beads; (B) zeta potential versus pH plot; (C) BET surface area; (D) pore size distribution of UiO-66/GOCOOH@SA composite beads.

from 2330 to 2344 cm^{-1} may be attributed to the formation of the −CO−Zr linkage.[55] The above mentioned evidence suggested the successful combination between the matrix components.

2.1.3. XRD. Figure 2B represents the XRD patterns of SA, GO, GOCOOH, UiO-66, and UiO-66/GOCOOH@SA composite beads. The XRD pattern clarifies that SA is most likely an amorphous polymer with no characteristic peaks, agreeing with previous studies.[56,57] Moreover, the XRD pattern of GO reveals the distinguishing peaks at 2θ = 10.4° corresponding to the (001) crystal plane, while the XRD pattern of GOCOOH shows upshifting the diffraction angle to 12.1°.[58,59] Furthermore, the XRD pattern of UiO-66 illustrates the main three characteristic peaks at 2θ = 7.4, 8.6, and 25.7° corresponding to the (111), (002), and (006) crystal planes, respectively.[42,60] The XRD pattern of the fabricated UiO-66/GOCOOH@SA composite beads manifests the main characteristic peaks of UiO-66. However, the characteristic peak of GOCOOH did not appear clearly in the XRD pattern of UiO-66/GOCOOH@SA, which is most likely due to the good distribution of GOCOOH in the beads, agreeing with the previous study by Eltaweil and his co-workers.[25] In addition, the relatively low intensities as suggested by the XRD pattern of UiO-66/GOCOOH@SA may be due to the combination of UiO-66 and GOCOOH with the amorphous SA.

2.1.4. TGA. Thermal behaviors of GO, GOCOOH, UiO-66, SA, and UiO-66/GOCOOH@SA composite beads were evaluated using thermogravimetric analysis (TGA) (Figure 2F). All TGA curves reveal a weight loss at 30 °C, which may be due to the evaporation of adsorbed water. For GO and GOCOOH, their TGA curves show a weight loss at 180 °C, which is attributed to the pyrolysis of oxygen-containing groups. Meanwhile, the weight loss at 250 °C is most likely due to the removal of more functional groups.[61] Finally, when the temperature exceeded 550 °C, COOH groups collapse.[62] For UiO-66, the TGA curve points out a weight loss at 100 °C, which is ascribed to the elimination of DMF molecules. In addition, a weight loss at 450 °C is assigned to the decomposition of UiO-66, resulting from the burn of the organic ligand.[42] For SA, the TGA curve shows two weight loss stages at 225 and 340 °C, which may be due to the tear of chains and monomers of SA, while the weight loss after 400 °C is due to the decomposition of SA.[63,64] The TGA profile of UiO-66/GOCOOH@SA composite beads suggests the enhanced thermal behavior of the fabricated beads.

2.1.5. Zeta Potential. The surface charge of the adsorbent plays a vital role in the adsorption process. So, it was an essential issue to scrutinize the surface charge of the fabricated UiO-66/GOCOOH@SA composite beads. Figure 3B shows the variation of the zeta potential of UiO-66/GOCOOH@SA composite beads with pH. Results demonstrated that UiO-66/GOCOOH@SA composite beads have a negative surface charge at all pH values; however, the magnitude of the surface charge increases with increasing pH, which could be attributed to the deprotonation of carboxyl groups. It is obvious that the ZP decreased sharply with increasing pH from 2 to 5; however, beyond pH 5, there is a slight decrease in the ZP of UiO-66/GOCOOH@SA composite beads where all carboxylate groups

https://doi.org/10.1021/acsomega.1c03479
ACS Omega 2021, 6, 23528−23541

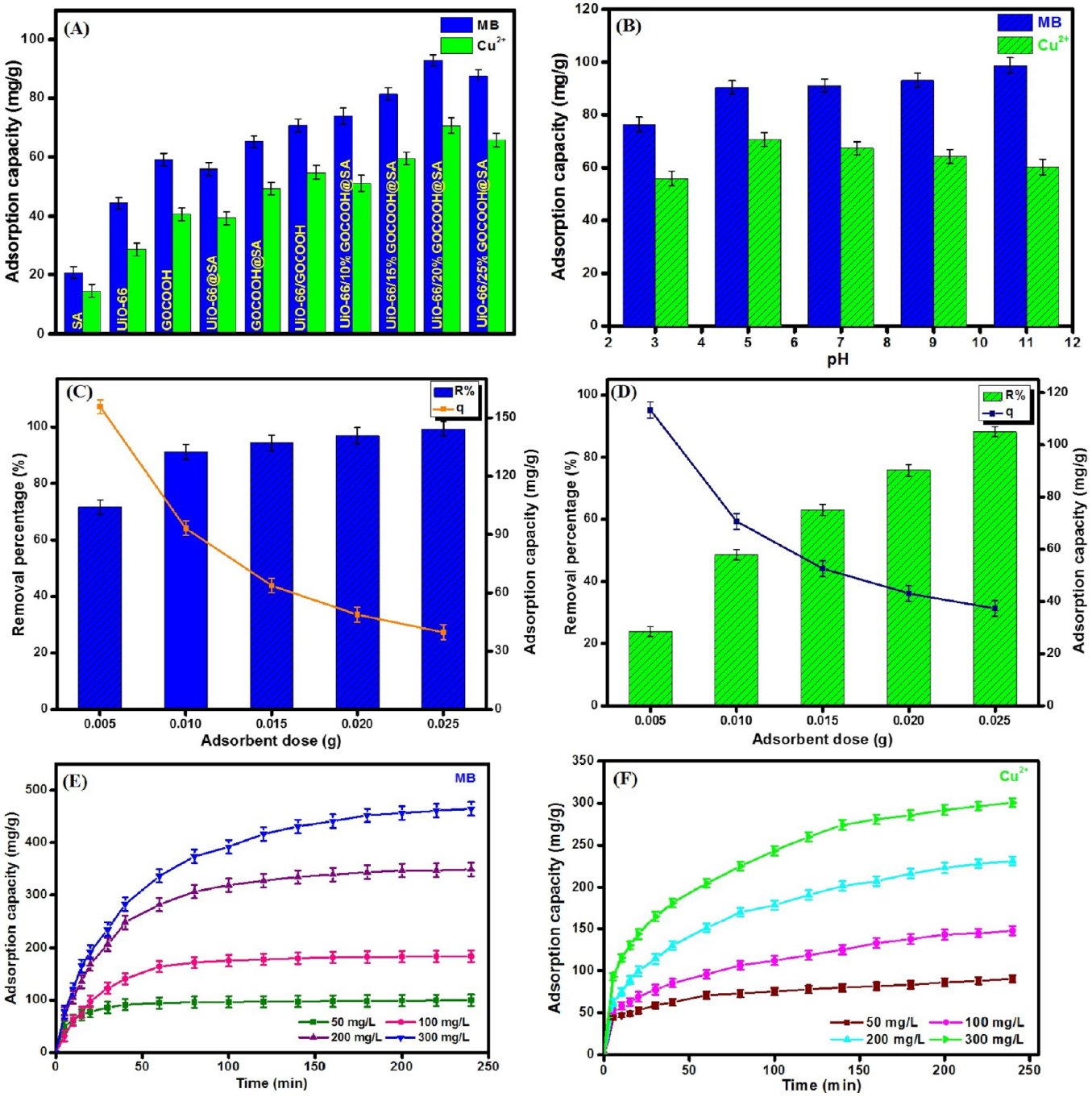

Figure 4. Effect of bead composition (A), pH (B), adsorbent dose (C, D), and initial concentration (E, F) on the adsorption capacity of MB and Cu^{2+} onto UiO-66/GOCOOH@SA composite beads.

are expected to be deprotonated. On this basis, UiO-66/GOCOOH@SA composite beads are a good candidate for the removal of cationic pollutants.

2.1.6. BET. The BET surface area and pore size distribution of UiO-66/GOCOOH@SA composite beads were measured utilizing the N_2 adsorption−desorption isotherm (Figure 3C,D). It is clear that there is a significant increment at a relatively low pressure (P/P_0 < 0.05 atm), asserting the microporous structure of the fabricated UiO-66/GOCOOH@SA composite beads. Moreover, the BET isotherm represents type-IV with a H_4 hysteresis loop, suggesting the presence of a mesoporous structure. Furthermore, it was recorded that the S_{BET} surface area was 54.75 m^2/g and the total pore volume was 0.0104 cm^3/g.

2.2. Adsorbability of UiO-66/GOCOOH@SA Composite Beads. *2.2.1. Impact of the GOCOOH Proportion.* It was found that the adsorption capacities of MB onto the pristine components UiO-66, GOCOOH, and SA beads were 44.59, 59.02, and 20.57 mg/g and those of Cu^{2+} were 28.98, 40.74, and 14.68 mg/g, respectively (Figure 4A). Furthermore, the results clarified that the incorporation of UiO-66 and GOCOOH in SA beads significantly increased their adsorption capacity for both MB and Cu^{2+} at which the adsorption capacities of MB and Cu^{2+} onto UiO-66@SA were 55.99 and 39.46 mg/g while those onto GOCOOH@SA were 65.12 and

https://doi.org/10.1021/acsomega.1c03479
ACS Omega 2021, 6, 23528−23541

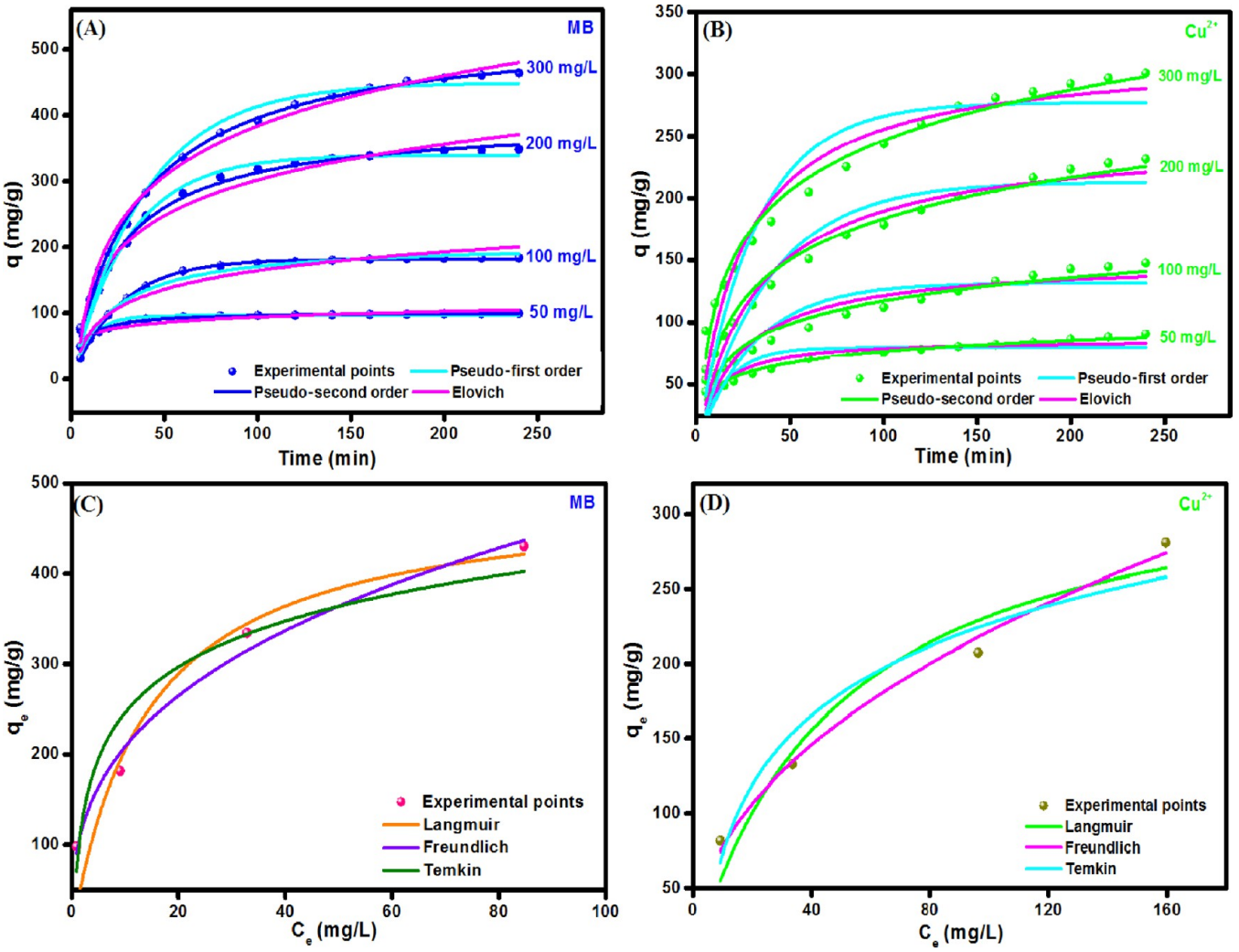

Figure 5. Kinetic models and isotherm models for the adsorption of MB (A, C) and Cu^{2+} (B, D) onto UiO-66/GOCOOH@SA composite beads.

49.64 mg/g, respectively. Furthermore, the increment in the GOCOOH proportion from 10 to 20 wt % boosted the adsorption capacity of both MB and Cu^{2+} onto UiO-66/GOCOOH@SA composite beads from 73.88 and 51.36 to 93.16 and 70.71 mg/g, respectively. However, the increase in GOCOOH proportion over 20 wt % led to a decrease in the adsorption capacity of both MB and Cu^{2+} from 93.16 and 70.71 to 87.87 and 65.73 mg/g, respectively. This observation is most likely due to the pore-blocking effect, as explained in the previous literature.[25,65] It was monitored that the adsorption capacities of the UiO-66/GOCOOH (20%) composite toward both MB and Cu^{2+} were 70.18 and 54.96 mg/g, respectively. This finding indicated that the encapsulation of UiO-66/GOCOOH into SA beads has dual benefits as it provided an easily separable adsorbent with enhanced adsorption capacity.

2.2.2. Impact of pH. As a matter of fact, pH solution dominates strongly on the surface charge of the adsorbent as well as the adsorbate ionization degree, thereby controlling the efficiency of the adsorption. Figure 4B points out that the increase in the pH of MB solution from 3 to 11 dramatically increases the adsorption capacity of MB onto UiO-66/GOCOOH@SA composite beads from 76.30 to 98.76 mg/g, respectively. On the other hand, the optimal adsorption capacity of Cu^{2+} occurs at pH 5 at which the adsorption capacity increases from 55.90 to 70.71 mg/g with the increase in pH from 3 to 5. This boost in the adsorption capacity of both MB and Cu^{2+} may be attributed to the fact that the increase in pH provides plenty of negative charges on the surface of the beads, which strengthens the electrostatic interaction between the cationic MB and the negatively charged UiO-66/GOCOOH@SA composite beads. Nevertheless, the dwindling of Cu^{2+}adsorption capacity at pH >5 may be due to Cu^{2+} precipitates in different hydroxide forms: $Cu(OH)^{+}$, $Cu(OH)_2$, $Cu_2(OH)_2^{2+}$, and $Cu(OH)_3^{-}$ at a highly alkaline medium.[66]

2.2.3. Impact of Adsorbent Dose. Figure 4C,D elucidates the impact of the increase in the dose of UiO-66/GOCOOH@SA composite beads from 0.005 to 0.025 g on the adsorption capacity of MB and Cu^{2+}. It is obvious that the increment in the bead dose leads to a decrease in the adsorption capacities of MB and Cu^{2+} from 155.72 and 113.30 to 39.78 and 37.31 mg/g, respectively, which may be ascribed to the aggregation of the particles. Contrariwise, the removal percentages of MB and Cu^{2+} increase from 71.66 and 23.99 to 99.28 and 88.22%, respectively, with increasing bead dose, which may be due to the increase in the number of active sites on the bead surface.

2.2.4. Impact of Initial Concentration. Figure 4E and Figure 4F represent the effect of the increase in the initial concentrations of both MB and Cu^{2+} on the adsorption

https://doi.org/10.1021/acsomega.1c03479
ACS Omega 2021, 6, 23528−23541

Table 1. Adsorption Kinetic Model Parameters of the Adsorption of Both MB and Cu^{2+} onto UiO-66/GOCOOH@SA Composite Beads

	concentration of MB				concentration of Cu^{2+}			
parameter	50	100	200	300	50	100	200	300
$q_{e,\,exp}$ (mg/g)	99.69	184.08	348.75	464.54	90.30	147.63	231.32	300.71
Pseudo 1st order								
$q_{e,\,cal}$ (mg/g)	86.62	178.48	330.03	449.48	79.34	131.58	213.13	277.17
k_1 (min^{-1})	0.101	0.037	0.032	0.025	0.067	0.032	0.026	0.032
R^2	0.922	0.993	0.990	0.986	0.655	0.780	0.906	0.871
Pseudo 2nd order								
$q_{e,\,cal}$ (mg/g)	102.31	207.75	393.42	536.53	92.68	149.93	249.97	317.09
k_1 (g/mg·min)	1.7×10^{-3}	2.22×10^{-4}	9.94×10^{-5}	5.25×10^{-5}	1.1×10^{-3}	2.86×10^{-4}	1.26×10^{-4}	1.13×10^{-4}
R^2	0.986	0.998	0.996	0.999	0.976	0.953	0.978	0.983
Elovich								
α (mg/g·min)	116.52	8.34	13.71	13.35	18.72	7.83	8.20	14.49
β (g/mg)	0.084	0.024	0.013	0.009	0.079	0.037	0.021	0.017
R^2	0.894	0.945	0.975	0.981	0.852	0.886	0.960	0.947

Table 2. Adsorption Isotherm Model Parameters of the Adsorption of Both MB and Cu^{2+} onto UiO-66/GOCOOH@SA Composite Beads

model	Langmuir			Freundlich			Temkin		
parameter	q_m (mg/g)	b (L/mg)	R^2	k_F (L/mg)	n	R^2	K_t (L/g)	b_t (kJ/mol)	R^2
MB	490.72	0.072	0.888	93.943	2.888	0.980	0.813	0.033	0.891
Cu^{2+}	343.49	0.024	0.899	27.253	2.198	0.986	0.158	0.037	0.904

capacity of the UiO-66/GOCOOH@SA composite beads, respectively. It is obvious that the increase in the initial concentrations of both MB and Cu^{2+} from 50 to 300 mg/g directly increases the adsorption capacity of UiO-66/GOCOOH@SA composite beads toward both MB and Cu^{2+} from 99.69 and 90.30 to 464.54 and 300.71 mg/g, respectively. This predictable result may be ascribed to the fact that increasing the initial concentrations of both pollutants leads to an increase in the driving force of MB molecules and Cu^{2+} ions toward the surface of UiO-66/GOCOOH@SA composite beads.[67]

2.3. Kinetics Study. The obtained experimental data were modeled by pseudo-first-order, pseudo-second-order, and Elovich models to explore the mechanism of both MB and Cu^{2+} onto the fabricated UiO-66/GOCOOH@SA composite beads. The following equations represent the non-linear forms of the applied kinetics.

$$q_t = q_e(1 - e^{-k_1 t}) \quad (1)$$

$$q_t = \frac{t k_2 q_e^2}{1 + t k_2 q_e} \quad (2)$$

$$q_t = \frac{1}{\beta} \ln(\alpha\beta t + 1) \quad (3)$$

where q_t and q_e are the amounts of Cr(VI) uptakes at time t and equilibrium, respectively. k_1 and k_2 are the rate constants of the pseudo-first order and pseudo-second order, respectively. α and β are Elovich coefficients that represent the initial adsorption rate and the desorption coefficient, respectively, which are also related to the extent of surface coverage and activation energy for chemisorption.

By inspecting the curves of the kinetic modes (Figure 5A,B) and the computed parameters (Table 1), we can deduce that the experimental data of the adsorption of both MB and Cu^{2+} onto UiO-66/GOCOOH@SA composite beads are well described by the pseudo-second order since the R^2 values of the pseudo-second-order model are higher than the pseudo-first-order and Elovich models. In addition, the q_{cal} values from the pseudo-second order are more analogous to the q_{exp} values. Moreover, the obtained parameters from the Elovich model suggest that the rate of both adsorption processes is higher than the desorption since the α values are larger than β values.

2.4. Isotherm Study. To infer the nature of the interaction of both MB and Cu^{2+} with UiO-66/GOCOOH@SA composite beads, the obtained equilibrium data were modeled by the Langmuir, Freundlich, and Temkin isotherm models (Figure 5C,D). The non-linear equations of these mentioned models are expressed by the following equations.

$$q_e = \frac{q_{max} K_L C_e}{1 + K_L C_e} \quad (4)$$

$$q_e = k_F C_e^{1/n} \quad (5)$$

$$q_e = \frac{RT}{b_T} \ln k_T C_e \quad (6)$$

where q_e and C_e are the adsorption capacity and the concentration of the unadsorbed Cr(VI) at equilibrium, respectively. q_m and K_L are the monolayer adsorption capacity and Langmuir constant, respectively. n and K_F are Freundlich constants. k_T is the equilibrium binding constant, and b is the Temkin constant related to the heat of adsorption. R is the gas constant (8.314 J/mol·K), and T is the absolute temperature.

Based on R^2 values (Table 2), the adsorption of both MB and Cu^{2+} onto UiO-66/GOCOOH@SA composite beads obeys the Freundlich isotherm model. Moreover, the maximum adsorption capacities of MB and Cu^{2+} onto UiO-66/GOCOOH@SA composite beads were 490.72 and 343.49 mg/g, respectively. Furthermore, the Temkin model suggested

https://doi.org/10.1021/acsomega.1c03479
ACS Omega 2021, 6, 23528−23541

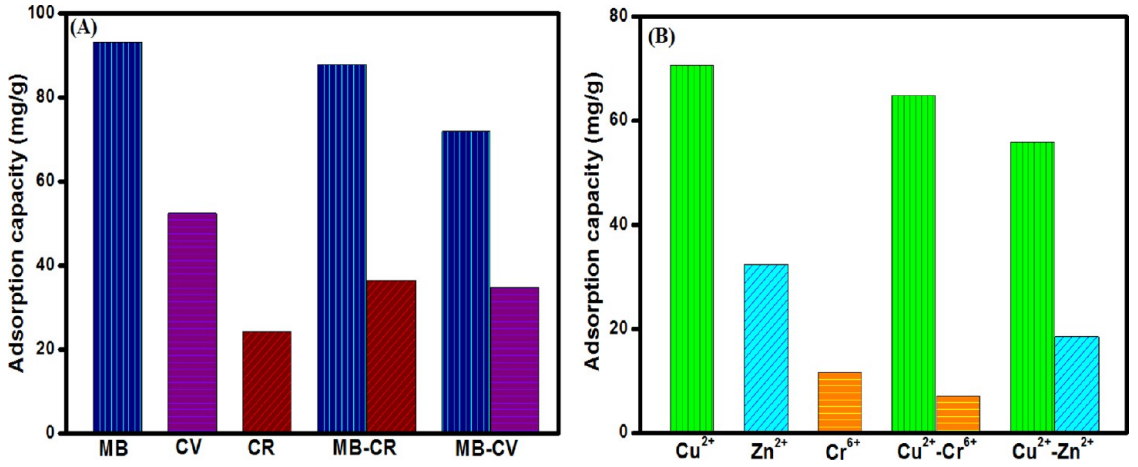

Figure 6. Impact of (A) interfering dyes on the adsorption of MB and (B) interfering metal ions on the adsorption of Cu^{2+} onto UiO-66/GOCOOH@SA composite beads.

Table 3. Comparison of Adsorption Capacity MB and Cu^{2+} onto the Developed UiO-66/GOCOOH@SA Composite Beads with Other Reported Adsorbents

pollutant	adsorbent	q_{max} (mg/g)	$q_{e,\ exp}$	pH	T (°C)	ref	year
MB dye	raw kaolin	52.76	44.70	6.0	25	69	2018
	xylan-gelatin cross-linked hydrogel	35.58	14.45	5.8	25	70	2021
	cross-linked agar/κ-carrageenan hydrogel	242.30	N/A	7.0	35	30	2020
	CMC/GOCOOH beads	183.32	180.23	10.0	25	49	2020
	UiO-66/MIL-101(Fe)-GOCOOH composite	448.71	439.36	9.0	25	25	2020
	UiO-66/GOCOOH@SA beads	476.19	464.54	9.0	25	this study	
Cu^{2+}	amidoxime-functionalized polyacrylamide-modified chitosan	190.70	164.80	5	25	71	2020
	porous COCB beads	227.27	92.13	5.0	30	72	2015
	EDA-functionalized magnetic cellulose nanocomposite	86.96	78.52	5.5	25	73	2019
	magnetic chitosan composite	216.60	N/A	5.5	25	2	2017
	UiO-66/GOCOOH@SA beads	322.58	300.71	5	25	this study	

the physical adsorption process of both MB and Cu^{2+} onto UiO-66/GOCOOH@SA composite beads. In addition, the adsorption preference of both MB and Cu^{2+} onto the beads was confirmed by the computed n value from the Freundlich model that was found to be larger than 2 in both adsorption processes.

2.5. Thermodynamics Study. To explicitly evaluate the effect of temperature on the nature of both the studied adsorption processes, thermodynamic parameters such as the Gibbs free energy (ΔG^0), standard enthalpy (ΔH^0), and standard entropy (ΔS^0) were computed by using the following equations:

$$\ln K_e = \frac{\Delta S^0}{R} - \frac{\Delta H^0}{RT} \quad (7)$$

$$\Delta G^o = \Delta H^0 - T\Delta S^0 \quad (8)$$

where K_e (thermodynamic equilibrium constant)$=\frac{C_{Ae}}{C_e}$. C_{Ae} is the concentration of MB and Cu^{2+} onto the surface of UiO-66/GOCOOH@SA composite beads. Meanwhile, C_e is the concentration of both MB and Cu^{2+} in solution at equilibrium. R is the gas constant, and T is the system temperature.

According to the ΔH^0 and ΔS^0 values of both the adsorption processes derived from the slope and intercept of van't Hoff plots (Table S1 and Figure S1A,B), the adsorptions of MB and Cu^{2+} onto UiO-66/GOCOOH@SA composite beads are endothermic processes with a high degree of randomness at the solution−solid interface. Furthermore, the negative ΔG^0 values indicate the spontaneity and thermodynamic favorability of both the adsorption process of MB and Cu^{2+} onto UiO-66/GOCOOH@SA composite beads.

2.6. Selectivity Study. Indeed, wastewater contains enormous amounts of dyes and heavy metals that fiercely compete for the adsorption sites of the adsorbent.[42] Hence, it was vital to evaluate the adsorption behavior of the fabricated UiO-66/GOCOOH@SA composite beads toward MB in the presence of the interfering anionic dye (CR) and cationic dye (CV) and Cu^{2+} in the presence of the coexisting metal cation (Zn^{2+}) and anion (Cr^{6+}), as depicted in Figure 6. It was found that UiO-66/GOCOOH@SA composite beads are more selective to MB (93.16 mg/g) than CV (52.45 mg/g) and CR (24.22 mg/g). In the case of the MB-CV binary system, the adsorption capacities of both MB and CV significantly dwindled from 93.16 and 52.45 to 71.93 to 34.73 mg/g, respectively, which is most likely due to the competition between the two cationic dyes for the binding sites of UiO-66/GOCOOH@SA composite beads. Meanwhile, the adsorption capacity of MB is slightly diminished in the existence of CR, inferring the selectivity of the beads toward MB. Nevertheless, the adsorption capacity of CR incremented in a binary system reached 36.54 mg/g, which may be attributed to the interaction of CR with MB, agreeing with the previous study by Bentahar and his co-workers.[68] Moreover, it was recorded that the adsorption capacities of Cu^{2+}, Zn^{2+}, and Cr^{6+} onto UiO-66/GOCOOH@SA composite beads were 70.71, 32.48,

https://doi.org/10.1021/acsomega.1c03479
ACS Omega 2021, 6, 23528−23541

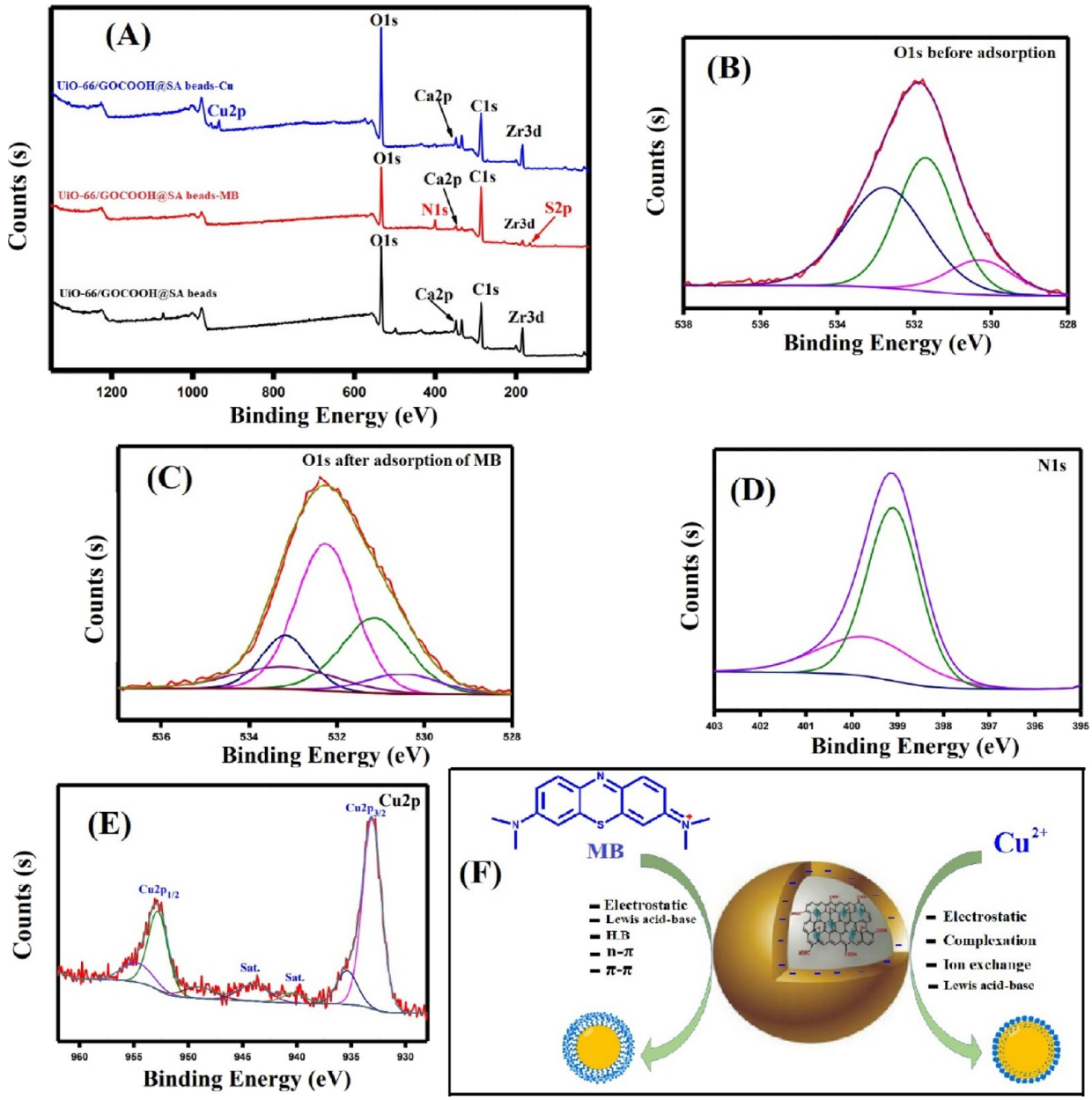

Figure 7. XPS spectra (A) wide spectrum of UiO-66/GOCOOH@SA composite beads before and after adsorption of MB and Cu^{2+}; (B, C) XPS high-resolution spectra of O 1s before and after adsorption of MB, (D) N 1s, and (E) Cu 2p; and (F) plausible mechanism for the adsorption of MB and Cu^{2+} onto UiO-66/GOCOOH@SA composite beads.

and 11.67 mg/g, respectively, reflecting the selectivity of the beads toward Cu^{2+}. A slight decrease in the adsorption capacity of Cu^{2+} in the presence of Cr^{6+} is most likely due to the repulsion forces between the negatively charged beads and the anionic Cr^{6+}. On the contrary, there was a significant decrease in the adsorption capacity of Cu^{2+} in the presence of Zn^{2+}, which may be ascribed to the competition between the cationic Cu^{2+} and Zn^{2+} for adsorbing on the negative surface of the beads.

2.7. Desorption Study. Without a shred of doubt, the regeneration ability of the adsorbent is an essential criterion to prove its viability in practical applications. Therefore, a reusability test was implemented for five adsorption/desorption cycles in both the studied adsorption processes. Figure S1C clarifies that the removal (%) of MB and Cu^{2+} after the fifth cycle decreased around 12 and 7%, respectively, asserting the excellent reusability and durability of the fabricated UiO-66/GOCOOH@SA composite beads.

2.8. Comparison with Other Adsorbents. Table 3 represents a comparative study between the synthesized UiO-66/GOCOOH@SA composite beads and other reported adsorbents in the previous literature to attest the excellent adsorption property of UiO-66/GOCOOH@SA composite beads toward the studied cationic contaminants. The prodigious adsorption capacity of both MB dye and Cu^{2+} ions onto the synthesized beads can be attributed to the synergistic effect between UiO-66, GOCOOH, and SA. In addition, the existence of extra carboxylic groups on the matrix of the beads provides plenty of negative charges, resulting in a strong attraction force between the negatively charged UiO-66/GOCOOH@SA composite beads and the cationic contaminants.

https://doi.org/10.1021/acsomega.1c03479
ACS Omega 2021, 6, 23528−23541

2.9. Adsorption Mechanism. XPS analysis was essentially utilized to further assert the successful combination between the pristine materials to form a matrix of UiO-66/GOCOOH@SA composite beads. Furthermore, it is a crucial issue to inspect the adsorption mechanism of both MB and Cu^{2+} onto the fabricated beads. The XPS wide spectrum (Figure 7A) illustrates the elemental composition of UiO-66/GOCOOH@SA composite beads: Zr 3d, C 1s, Ca 2p, and O 1s. The wide spectrum of UiO-66/GOCOOH@SA composite beads after the adsorption of MB (Figure 7A) confirms the appearance of two new peaks at 400.11 and 165.18 eV, which correspond to the N and S elements of MB, respectively. In addition, the high-resolution spectrum of O 1s before and after the adsorption of MB (Figure 7B,C) demonstrates shifting in the binding energy of the peaks from 532.92 to 532.86 eV, confirming the adsorption of MB onto UiO-66/GOCOOH@SA composite beads. In addition, the high-resolution spectrum of N 1s (Figure 7D) manifests a distinctive peak of $-N(CH_3)_2$ at 399.37 eV, which is one more evidence to confirm the MB adsorption onto UiO-66/GOCOOH@SA composite beads. It was reported that the adsorption of MB onto MOF materials occurs via the Lewis acid−base interaction.[74] Hence, the adsorption of MB onto UiO-66-based composite beads occurs via the interaction between the Lewis acid Zr sites and Lewis base $-N(CH_3)_2$ and $-C_6H_5$ groups since the molecules of MB are too large to entirely enter through the tight pores of the MOF. However, the pores of UiO-66 are loose enough for $-N(CH_3)_2$ and $-C_6H_5$ groups, so MB can partially enter the pores of UiO-66. Moreover, the adsorption mechanism of MB onto UiO-66/GOCOOH@SA composite beads may occur via electrostatic interactions between the cationic MB and the highly negative charged (reached −33 mV) UiO-66/GOCOOH@SA composite beads as clarified from the zeta potential result. In addition to the $\pi-\pi$ interaction, the n$-\pi$ interaction and van der Waals force vastly contribute to the MB adsorption mechanism into the fabricated UiO-66/GOCOOH@SA composite beads.[75,76]

On the other hand, the wide spectrum of UiO-66/GOCOOH@SA composite beads after the adsorption of Cu^{2+} shows a new peak at 934.5 eV, which is related to Cu 2p.[77] Furthermore, a noticeable decrease in the Ca 2p peak intensity suggests that Ca^{2+} is partially replaced by Cu^{2+} at which it is denoted in the previous literature that the adsorptive removal mechanism of heavy metals (e.g., Cu^{2+}, Cr^{3+}, Pb^{2+}, and Au^{3+}) onto SA occurs via the ion-exchange mechanism.[76] In addition, the high-resolution spectrum of Cu 2p (Figure 7E) reveals the distinguishing peaks of $2p_{1/2}$ and $2p_{3/2}$ at around 952.9 and 933.1 eV, respectively, indicating the formation of the $-OH-Cu^{2+}$ or $-O-Cu^{2+}$ complex.[78] In addition, the electrostatic interaction is a substantial mechanism of the Cu^{2+}adsorption process since the cationic Cu^{2+} strongly attracts to the oxygen-containing functional groups of the bead matrix.[79,80] To sum up, the adsorption mechanism of MB onto UiO-66/GOCOOH@SA composite beads takes place via electrostatic, Lewis acid−base, HB, n$-\pi$, and $\pi-\pi$ interactions while that of Cu^{2+} occurs via the synergistic effect of ion-exchange, complexation, and electrostatic interactions (Figure 7F). These findings are consistent with kinetics and isotherm studies that suggested that the adsorption of both MB and Cu^{2+} onto UiO-66/GOCOOH@SA composite beads occurs via chemisorption and physisorption.

3. CONCLUSIONS

A simple route for the incorporation UiO-66 MOF and GOCOOH into SA beads to form UiO-66/GOCOOH@SA composite beads was reported. Results confirmed that the fabricated beads could efficiently remove MB through electrostatic, HB, Lewis acid−base, $\pi-\pi$, and n$-\pi$ interactions. However, electrostatic, ion exchange, and complexation were the main mechanisms for the adsorption of Cu^{2+} ions. Furthermore, the modification of UiO-66@SA beads with GOCOOH greatly enhances the adsorption property of the fabricated MOF beads. Based on these results, the fabricated UiO-66/GOCOOH@SA composite beads are a promising candidate for the removal of cationic pollutants from wastewater, which could inspire researchers to develop novel adsorbents with exceptional characteristics.

4. EXPERIMENTAL SECTION

4.1. Materials. Graphite powder was provided from Alpha Chemika. Zirconium oxychloride, 1,4-benzene dicarboxylic acid, copper sulfate, and methylene blue were purchased from MP Biomedicals, LLC. Sodium alginate was used as received (M/G ratio of the alginate = 1.5, M_w = 6.4 × 104 g/mol, viscosity: 200 ± 20 mPa·s 1% wt (25 °C), Shanghai McLean Biochemical Technology Co., Ltd., China). Hydrogen peroxide, chloroacetic acid, *N*,*N*-dimethyl formamide, and hydrochloric acid were bought from Loba Chemie. Potassium permanganate, methanol, and ethanol were supplied by Aladdin Reagent Co., Ltd. Sodium hydroxide, calcium chloride, sodium nitrate, and sulfuric acid were obtained from Sinopharm Chemical Reagents.

4.2. Synthesis of Carboxylated Graphene Oxide. At first, GO was synthesized via Hummer's method.[25] Then, GOCOOH was synthesized as follows: 0.2 g of GO was dispersed into 100 mL of distilled water and stirred for 15 min. 5 g of NaOH and 5 g of Cl-CH_2COOH were mixed with the suspension and then sonicated for 3 h. Thereafter, an aqueous solution of HCl (10%) was added drop by drop until the pH of the reaction mixture was ∼7. Finally, the product was separated by centrifugation, then washed with distilled water, and dried at 60 °C for 6 h.

4.3. Synthesis of UiO-66. UiO-66 was synthesized according the method that was described in our previous literature with slight modifications.[42] Exactly, 0.322 g of $ZrOCl_2$ and 0.162 g of H_2BDC were dissolved into DMF under vigorous stirring for 60 min. After that, the reaction mixture was transferred into 100 mL of a Teflon-sealed autoclave and kept at 120 °C for 20 h. After the autoclave was cooled down to room temperature, the solid was separated by centrifugation, washed with DMF and ethanol, and then dried at 100 °C for 6 h.

4.4. Fabrication of UiO-66/GOCOOH@SA Composite Beads Adsorbents. UiO-66 (0.5 g) and GOCOOH (10, 15, 20, and 25 wt %) were dispersed into 5 mL of distilled water and sonicated for 2 h to ensure the formation of a homogeneous UiO-66/GOCOOH composite. In another container, 0.5 g of SA was thoroughly dissolved in 5 mL of distilled water under mechanical stirring. Then, the UiO-66/GOCOOH composite was added to the SA solution bit by bit and the mixture solution was kept under continuous stirring. After 2 h, the mixture was slowly added using a syringe into a 300 mL gelling solution of $CaCl_2$. Finally, UiO-66/GOCOOH@SA composite beads were washed with distilled

https://doi.org/10.1021/acsomega.1c03479
ACS Omega 2021, 6, 23528−23541

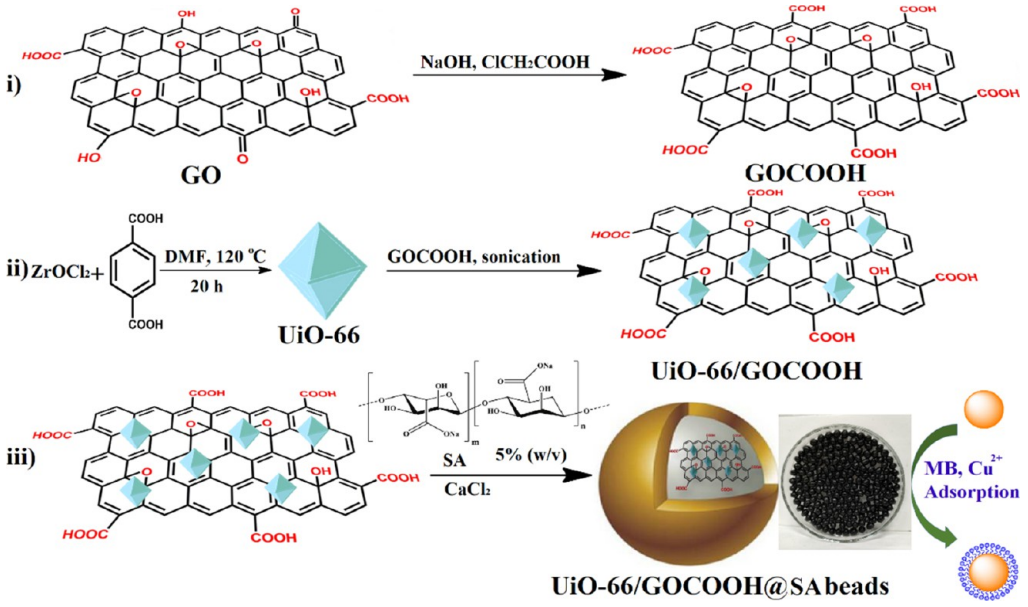

Figure 8. Schematic representation for the fabrication of the UiO-66/GOCOOH@SA composite bead adsorbent.

water. SA beads were fabricated with the same procedure without the addition of UiO-66 and GOCOOH.

4.5. Batch Experiment. The adsorption property of UiO-66/GOCOOH@SA composite beads toward MB dye and Cu^{2+} ions was evaluated using a batch experiment. For investigating the impact of adsorbent dosage on the adsorption process of both MB and Cu^{2+}, a variable dosage of UiO-66/GOCOOH@SA composite beads ranging from 0.005 to 0.025 g was soaked into a 20 mL aqueous solution of MB or Cu^{2+} with an initial concentration of 50 mg/L. Meanwhile, the impact of the pH medium was estimated at a range of 3 to 11 since the pH solution was adjusted with a 0.01 M aqueous solution of NaOH or HCl. In addition, the adsorption isotherms were assessed by soaking 0.01 g of UiO-66/GOCOOH@SA composite beads into MB or Cu^{2+} (V = 20 mL, C_0 = 50−300 mg/L). In addition, the adsorption of both MB and Cu^{2+} onto UiO-66/GOCOOH@SA composite beads was executed at diverse temperatures from 25 to 55 °C to find out the impact of the system temperature on the process efficiency. After each experiment, MB residual concentration was measured spectrophotometrically at 664 nm, while the residual concentration of Cu^{2+} was detected by an atomic absorption spectrophotometer. Adsorption capacity (q) and removal percent (R%) are computed from eqs 9 and 10, respectively.

$$q_t = \frac{(C_0 - C_t) \times V}{W} \tag{9}$$

$$R\% = \frac{C_0 - C_t}{C_0} \times 100 \tag{10}$$

where C_t and C_0 are the MB or Cu^{2+} concentration at time t and zero, respectively. Meanwhile, V and W are the volume of MB or Cu^{2+} and the weight of UiO-66/GOCOOH@SA composite beads, respectively.

Figure 8 shows a diagrammatic scheme for the fabrication steps of UiO-66/GOCOOH@SA composite beads and their application in the removal of both MB and Cu^{2+} from their aqueous solutions.

4.6. Selectivity Study. The selectivity of UiO-66/GOCOOH@SA composite beads toward MB was tested in the existence of the cationic crystal violet (CV) and the anionic Congo red (CR) as well as Cu^{2+} in the presence of metal cation Zn^{2+} and anion Cr^{6+}. The test was carried out as follows: 0.01 g of UiO-66/GOCOOH@SA composite beads was added to 20 mL of single-pollutant and multipollutant systems; then, UiO-66/GOCOOH@SA composite beads were collected and the concentration of residual dyes was measured via a spectrophotometer (λ_{max} (CR) = 500 nm and λ_{max} (CV) = 598 nm). Meanwhile, residual concentrations of Cu^{2+}, Zn^{2+}, and Cr^{6+} were measured by an atomic absorption spectrophotometer.

4.7. Recyclability Test. Basically, the recyclability test is an imperative index used to prove the viability of any suggested study. So, an expanded study was accomplished for five adsorption/desorption cycles to assess the reusability of the fabricated UiO-66/GOCOOH@SA composite beads. Desorption of both MB dye and Cu^{2+} ions from UiO-66/GOCOOH@SA was executed as follows. After each adsorption run, UiO-66/GOCOOH@SA−MB and UiO-66/GOCOOH@SA−Cu^{2+} were collected and soaked in ethanol and 0.1 mol/L HCl, respectively, under gentle stirring for 2 h. Then, UiO-66/GOCOOH@SA composite beads were reused in the next adsorption run.

4.8. Characterization. Bountiful characterization tools were utilized to confirm the successful fabrication of UiO-66/GOCOOH@SA composite beads as well as study their characteristics. Fourier transform infrared spectra (PerkinElmer Spectrum GX) were used to assert the chemical composition of UiO-66/GOCOOH@SA composite beads, while their crystal phase was investigated by an X-ray diffractometer (MAC Science M03XHF) with wavelength λ = 1.54 A° (Cu Kα), at a tube voltage of 35 kV and tube current of 30 mA. Moreover, the elemental composition of the fabricated UiO-66/GOCOOH@SA composite beads was assured by X-ray photoelectron spectroscopy (XPS; Thermo Scientific ESCALAB 250Xi VG). Scanning electron microscopy (SEM; JEOL JSM 6360 LA) pointed out the morphology of UiO-66/GOCOOH@SA composite beads. The sample was prepared as

https://doi.org/10.1021/acsomega.1c03479
ACS Omega 2021, 6, 23528−23541

follows: 5 mg of the analyzed sample was dispersed in 10 mL of ethanol for 6 h. Then, a few drops of the obtained suspension were put onto a grid coated with copper. Moreover, the surface charge of UiO-66/GOCOOH@SA composite beads was precisely determined by a zeta potential analyzer (Malvern, UK). The sample was prepared by grinding the beads to fine powder using a mortar and pestle. Then, a diluted suspension from the beads was prepared followed by adjusting the suspension pH at a range of 2−11 and sonicated for 1 h. The thermal properties of GO, GOCOOH, SA, UiO-66, and UiO-66/GOCOOH@SA composite beads were determined by a thermogravimetric analyzer (PerkinElmer, STA 6000 analyzer). In addition, the specific surface area of UiO-66/GOCOOH@SA composite beads was determined using the Brunauer−Emmett−Teller method (BET-Beckman Coulter, SA3100, USA). The sample was degassed for 3 h at 100 °C before the test.

■ ASSOCIATED CONTENT

Supporting Information

The Supporting Information is available free of charge at https://pubs.acs.org/doi/10.1021/acsomega.1c03479.

Adsorption thermodynamic parameters of the adsorption of both MB and Cu^{2+} onto UiO-66/GOCOOH@SA composite beads (Table S1) and van't Hoff plots and the reusability for the adsorption of MB and Cu^{2+} onto UiO-66/GOCOOH@SA composite beads (Figure S1) (PDF)

■ AUTHOR INFORMATION

Corresponding Author

Abdelazeem S. Eltaweil − *Chemistry Department, Faculty of Science, Alexandria University, Alexandria 21321, Egypt;* orcid.org/0000-0001-8912-1244; Email: abdelazeemeltaweil@alexu.edu.eg

Authors

Injy M. Mamdouh − *Chemistry Department, Faculty of Science, Alexandria University, Alexandria 21321, Egypt*

Eman M. Abd El-Monaem − *Chemistry Department, Faculty of Science, Alexandria University, Alexandria 21321, Egypt*

Gehan M. El-Subruiti − *Chemistry Department, Faculty of Science, Alexandria University, Alexandria 21321, Egypt*

Complete contact information is available at: https://pubs.acs.org/10.1021/acsomega.1c03479

Notes

The authors declare no competing financial interest.

■ REFERENCES

(1) Eltaweil, A. S.; Ali Mohamed, H.; Abd El-Monaem, E. M.; El-Subruiti, G. M. Mesoporous magnetic biochar composite for enhanced adsorption of malachite green dye: Characterization, adsorption kinetics, thermodynamics and isotherms. *Adv. Powder Technol.* **2020**, *31* (3), 1253.

(2) Li, J.; Jiang, B.; Liu, Y.; Qiu, C.; Hu, J.; Qian, G.; Guo, W.; Ngo, H. H. Preparation and adsorption properties of magnetic chitosan composite adsorbent for Cu^{2+} removal. *J. Cleaner Prod.* **2017**, *158*, 51−58.

(3) Duan, C.; Meng, X.; Liu, C.; Lu, W.; Liu, J.; Dai, L.; Wang, W.; Zhao, W.; Xiong, C.; Ni, Y. Carbohydrates-rich corncobs supported metal-organic frameworks as versatile biosorbents for dye removal and microbial inactivation. *Carbohydr. Polym.* **2019**, *222*, 115042.

(4) Lei, L.; Peng, Z.; Liang, T.; Yu, H.-R.; Cheng, C.-J. Solvothermal synthesis of poly(acrylic acid) decorated magnetic molybdenum disulfide nanosheets for highly-efficient adsorption of cationic dyes from aqueous solutions. *RSC Adv.* **2021**, *11*, 16490−16499.

(5) Hu, C.; Shen, J.-J.; Chang, A.-L.; Wei, T.-C. Microwave plasma torch synthesis of Zn-Al oxides as adsorbent and photocatalyst for organic compounds removal. *Powder Technol.* **2019**, *344*, 454−462.

(6) Wahlström, N.; Steinhagen, S.; Toth, G.; Pavia, H.; Edlund, U. Ulvan dialdehyde-gelatin hydrogels for removal of heavy metals and methylene blue from aqueous solution. *Carbohydr. Polym.* **2020**, *249*, 116841.

(7) Omer, A. M.; Elgarhy, G. S.; El-Subruiti, G. M.; Khalifa, R. E.; Eltaweil, A. S. Fabrication of novel iminodiacetic acid-functionalized carboxymethyl cellulose microbeads for efficient removal of cationic crystal violet dye from aqueous solutions. *Int. J. Biol. Macromol.* **2020**, *148*, 1072−1083.

(8) Oveisi, M.; Asli, M. A.; Mahmoodi, N. M. MIL-Ti metal-organic frameworks (MOFs) nanomaterials as superior adsorbents: Synthesis and ultrasound-aided dye adsorption from multicomponent wastewater systems. *J. Hazard. Mater.* **2018**, *347*, 123−140.

(9) Eltaweil, A. S.; Abd El-Monaem, E. M.; Omer, A. M.; Khalifa, R. E.; Abd El-Latif, M. M.; El-Subruiti, G. M. Efficient removal of toxic methylene blue (MB) dye from aqueous solution using a metal-organic framework (MOF) MIL-101 (Fe): isotherms, kinetics, and thermodynamic studies. *Desalin. Water Treat.* **2020**, *189*, 395−407.

(10) Hamedi, A.; Zarandi, M. B.; Nateghi, M. R. Highly efficient removal of dye pollutants by MIL-101(Fe) metal-organic framework loaded magnetic particles mediated by Poly L-Dopa. *J. Environ. Chem. Eng.* **2019**, *7*, 102882.

(11) Hong, M.; Yu, L.; Wang, Y.; Zhang, J.; Chen, Z.; Dong, L.; Zan, Q.; Li, R. Heavy metal adsorption with zeolites: The role of hierarchical pore architecture. *Chem. Eng. J.* **2019**, *359*, 363−372.

(12) Vakili, M.; Deng, S.; Cagnetta, G.; Wang, W.; Meng, P.; Liu, D.; Yu, G. Regeneration of chitosan-based adsorbents used in heavy metal adsorption: A review. *Sep. Purif. Technol.* **2019**, *224*, 373−387.

(13) Zhu, Y.; Fan, W.; Zhang, K.; Xiang, H.; Wang, X. Nano-manganese oxides-modified biochar for efficient chelated copper citrate removal from water by oxidation-assisted adsorption process. *Sci. Total Environ.* **2020**, *709*, 136154.

(14) Yang, Z.; Li, M.; Yu, M.; Huang, J.; Xu, H.; Zhou, Y.; Song, P.; Xu, R. A novel approach for methylene blue removal by calcium dodecyl sulfate enhanced precipitation and microbial flocculant GA1 flocculation. *Chem. Eng. J.* **2016**, *303*, 1−13.

(15) Ren, Y.; Li, T.; Zhang, W.; Wang, S.; Shi, M.; Shan, C.; Zhang, W.; Guan, X.; Lv, L.; Hua, M.; Pan, B. MIL-PVDF blend ultrafiltration membranes with ultrahigh MOF loading for simultaneous adsorption and catalytic oxidation of methylene blue. *J. Hazard. Mater.* **2019**, *365*, 312−321.

(16) Pan, X.; Cheng, S.; Su, T.; Zuo, G.; Zhao, W.; Qi, X.; Wei, W.; Dong, W. Fenton-like catalyst Fe_3O_4@ polydopamine-MnO_2 for enhancing removal of methylene blue in wastewater. *Colloids Surf., B* **2019**, *181*, 226−233.

(17) Nyankson, E.; Efavi, J. K.; Agyei-Tuffour, B.; Manu, G. Synthesis of TiO_2−Ag_3PO_4 photocatalyst material with high adsorption capacity and photocatalytic activity: application in the removal of dyes and pesticides. *RSC Adv.* **2021**, *11*, 17032−17045.

(18) Dong, W.; Wang, D.; Wang, H.; Li, M.; Chen, F.; Jia, F.; Yang, Q.; Li, X.; Yuan, X.; Gong, J.; Li, H.; Ye, J. Facile synthesis of In2S3/UiO-66 composite with enhanced adsorption performance and photocatalytic activity for the removal of tetracycline under visible light irradiation. *J. Colloid Interface Sci.* **2019**, *535*, 444−457.

(19) Hosny, M.; Fawzy, M.; Abdelfatah, A. M.; Fawzy, E. E.; Eltaweil, A. S. Comparative study on the potentialities of two halophytic species in the green synthesis of gold nanoparticles and their anticancer, antioxidant and catalytic efficiencies. *Adv. Powder Technol.* **2021**, *32* (9), 3220−3233.

(20) El-Borady, O. M.; Fawzy, M.; Hosny, M. Antioxidant, anticancer and enhanced photocatalytic potentials of gold nano-

particles biosynthesized by common reed leaf extract. *Appl. Nanosci.* **2021**, 1−12.
(21) Hosny, M.; Fawzy, M.; El-Borady, O. M.; Mahmoud, A. E. D. Comparative study between Phragmites australis root and rhizome extracts for mediating gold nanoparticles synthesis and their medical and environmental applications. *Adv. Powder Technol.* **2021**, *32*, 2268−2279.
(22) Abd El-Monaem, E. M.; Abd El-Latif, M. M.; Eltaweil, A. S.; El-Subruiti, G. M. Cobalt Nanoparticles Supported on Reduced Amine-Functionalized Graphene Oxide for Catalytic Reduction of Nitroanilines and Organic Dyes. *NANO* **2021**, *16*, 2150039.
(23) El-Subruiti, G.; Eltaweil, A. S.; Sallam, S. A. Synthesis of active MFe_2O_4/γ-Fe_2O_3 nanocomposites (metal= Ni or Co) for reduction of nitro-containing pollutants and methyl orange degradation. *NANO* **2019**, *14*, 1950125.
(24) El Bestawy, E.; El-Shatby, B. F.; Eltaweil, A. S. Integration between bacterial consortium and magnetite (Fe_3O_4) nanoparticles for the treatment of oily industrial wastewater. *World J. Microbiol. Biotechnol.* **2020**, *36*, 141.
(25) Eltaweil, A. S.; Abd El-Monaem, E. M.; El-Subruiti, G. M.; Abd El-Latif, M. M.; Omer, A. M. Fabrication of UiO-66/MIL-101(Fe) binary MOF/carboxylated-GO composite for adsorptive removal of methylene blue dye from aqueous solutions. *RSC Adv.* **2020**, *10*, 19008−19019.
(26) Li, X.; Yu, X.; Liu, L.; Yang, J.; Liu, S.; Zhang, T. Preparation, characterization serpentine-loaded hydroxyapatite and its simultaneous removal performance for fluoride, iron and manganese. *RSC Adv.* **2021**, *11*, 16201−16215.
(27) Davoodi, M.; Davar, F.; Rezayat, M. R.; Jafari, M. T.; Bazarganipour, M.; Shalan, A. E. Synthesis and characterization of a new ZIF-67@$MgAl_2O_4$ nanocomposite and its adsorption behaviour. *RSC Adv.* **2021**, *11*, 13245−13255.
(28) El-Sayed, E. M.; Tamer, T. M.; Omer, A. M.; Mohy Eldin, M. S. Development of novel chitosan schiff base derivatives for cationic dye removal: Methyl orange model. *Desalin. Water Treat.* **2016**, *57*, 22632−22645.
(29) Hoslett, J.; Ghazal, H.; Mohamad, N.; Jouhara, H. Removal of methylene blue from aqueous solutions by biochar prepared from the pyrolysis of mixed municipal discarded material. *Sci. Total Environ.* **2020**, *714*, 136832.
(30) Duman, O.; Polat, T. G.; Diker, C. Ö.; Tunç, S. Agar/κ-carrageenan composite hydrogel adsorbent for the removal of methylene blue from water. *Int. J. Biol. Macromol.* **2020**, *160*, 823−835.
(31) Tabatabaeian, R.; Dinari, M.; Aliabadi, H. M. Cross-linked bionanocomposites of hydrolyzed guar gum/magnetic layered double hydroxide as an effective sorbent for methylene blue removal. *Carbohydr. Polym.* **2021**, *257*, 117628.
(32) Dinari, M.; Tabatabaeian, R. Ultra-fast and highly efficient removal of cadmium ions by magnetic layered double hydroxide/guargum bionanocomposites. *Carbohydr. Polym.* **2018**, *192*, 317−326.
(33) Kausar, A.; Sher, F.; Hazafa, A.; Javed, A.; Sillanpää, M.; Iqbal, M. Biocomposite of sodium-alginate with acidified clay for wastewater treatment: Kinetic, equilibrium and thermodynamic studies. *Int. J. Biol. Macromol.* **2020**, *161*, 1272−1285.
(34) Omer, A. M.; Ahmed, M. S.; El-Subruiti, G. M.; Khalifa, R. E.; Eltaweil, A. S. pH-Sensitive Alginate/Carboxymethyl Chitosan/Aminated Chitosan Microcapsules for Efficient Encapsulation and Delivery of Diclofenac Sodium. *Pharmaceutics* **2021**, *13*, 338.
(35) Eldin, M. M.; Hashem, A.; Tamer, T.; Omer, A.; Yossuf, M.; Sabet, M. Development of cross linked chitosan/alginate polyelectrolyte proton exchanger membranes for fuel cell applications. *Int. J. Electrochem. Sci.* **2017**, *12*, 3840−3858.
(36) Gokila, S.; Gomathi, T.; Sudha, P. N.; Anil, S. Removal of the heavy metal ion chromiuim(VI) using Chitosan and Alginate nanocomposites. *Int. J. Biol. Macromol.* **2017**, *104*, 1459−1468.
(37) Nguyen, T.-D.; Dang, C.-H.; Mai, D.-T. Biosynthesized AgNP capped on novel nanocomposite 2-hydroxypropyl-β-cyclodextrin/alginate as a catalyst for degradation of pollutants. *Carbohydr. Polym.* **2018**, *197*, 29−37.
(38) Wang, B.; Wan, Y.; Zheng, Y.; Lee, X.; Liu, T.; Yu, Z.; Huang, J.; Ok, Y. S.; Chen, J.; Gao, B. Alginate-based composites for environmental applications: a critical review. *Crit. Rev. Environ. Sci. Technol.* **2019**, *49*, 318−356.
(39) Kaur, H.; Mohanta, G. C.; Gupta, V.; Kukkar, D.; Tyagi, S. Synthesis and characterization of ZIF-8 nanoparticles for controlled release of 6-mercaptopurine drug. *J. Drug Delivery Sci. Technol.* **2017**, *41*, 106−112.
(40) González, C. M. O.; Kharisov, B. I.; Kharissova, O. V.; Quezada, T. E. S. Synthesis and applications of MOF-derived nanohybrids: A review. *Mater. Today: Proc.* **2021**, *46*, 3018−3029.
(41) Ma, M.; Bi, Y.; Tong, Z.; Liu, Y.; Lyu, P.; Wang, R.; Ma, Y.; Wu, G.; Liao, Z.; Chen, Y. Recent progress of MOF-derived porous carbon materials for microwave absorption. *RSC Adv.* **2021**, *11*, 16572−16591.
(42) Eltaweil, A. S.; Elshishini, H. M.; Ghatass, Z. F.; Elsubruiti, G. M. Ultra-high adsorption capacity and selective removal of Congo red over aminated graphene oxide modified Mn-doped UiO-66 MOF. *Powder Technol.* **2021**, *379*, 407−416.
(43) Jia, X.; Zhang, B.; Chen, C.; Fu, X.; Huang, Q. Immobilization of chitosan grafted carboxylic Zr-MOF to porous starch for sulfanilamide adsorption. *Carbohydr. Polym.* **2021**, *253*, 117305.
(44) Omer, A. M.; Abd El-Monaem, E. M.; Abd El-Latif, M. M.; El-Subruiti, G. M.; Eltaweil, A. S. Facile Fabrication of Novel Magnetic ZIF-67 MOF@Aminated Chitosan Composite Beads for the Adsorptive Removal of Cr(VI) from Aqueous Solutions. *Carbohydr. Polym.* **2021**, *265*, 118084.
(45) Arabkhani, P.; Javadian, H.; Asfaram, A.; Ateia, M. Decorating graphene oxide with zeolitic imidazolate framework (ZIF-8) and pseudo-boehmite offers ultra-high adsorption capacity of diclofenac in hospital effluents. *Chemosphere* **2021**, *271*, 129610.
(46) ElSawy, A. M.; Attia, N. F.; Mohamed, H. I.; Mohsen, M.; Talaat, M. H. Innovative coating based on graphene and their decorated nanoparticles for medical stent applications. *Mater. Sci. Eng.: C* **2019**, *96*, 708−715.
(47) An, Y.; Zheng, H.; Zheng, X.; Sun, Q.; Zhou, Y. Use of a floating adsorbent to remove dyes from water: a novel efficient surface separation method. *J. Hazard. Mater.* **2019**, *375*, 138−148.
(48) Karthikeyan, P.; Elanchezhiyan, S. S. D.; Banu, H. A. T.; Farzana, M. H.; Park, C. M. Hydrothermal synthesis of hydroxyapatite-reduced graphene oxide (1D−2D) hybrids with enhanced selective adsorption properties for methyl orange and hexavalent chromium from aqueous solutions. *Chemosphere* **2021**, *276*, 130200.
(49) Eltaweil, A. S.; Elgarhy, G. S.; El-Subruiti, G. M.; Omer, A. M. Carboxymethyl cellulose/carboxylated graphene oxide composite microbeads for efficient adsorption of cationic methylene blue dye. *Int. J. Biol. Macromol.* **2020**, *154*, 307−318.
(50) Elnashar, M. M.; Yassin, M. A.; Moneim, A. E.-F. A.; Bary, E. A. Investigating the Unexpected Behavior for the Release Kinetics of Brilliant Blue Encapsulated into Calcium Alginate Beads. *Eurasian Chem.-Technol. J.* **2015**, *12*, 130200.
(51) Yang, S.-T.; Chen, S.; Chang, Y.; Cao, A.; Liu, Y.; Wang, H. Removal of methylene blue from aqueous solution by graphene oxide. *J. Colloid Interface Sci.* **2011**, *359*, 24−29.
(52) Bach, L. G.; Van Tran, T.; Nguyen, T. D.; Van Pham, T.; Do, S. T. Enhanced adsorption of methylene blue onto graphene oxide-doped XFe_2O_4 (X= Co, Mn, Ni) nanocomposites: kinetic, isothermal, thermodynamic and recyclability studies. *Res. Chem. Intermed.* **2018**, *44*, 1661−1687.
(53) Alqadami, A. A.; Naushad, M.; Abdalla, M. A.; Khan, M. R.; Alothman, Z. A. Adsorptive removal of toxic dye using Fe3O4−TSC nanocomposite: equilibrium, kinetic, and thermodynamic studies. *J. Chem. Eng. Data* **2016**, *61*, 3806−3813.
(54) Kong, Y.; Zhuang, Y.; Han, K.; Shi, B. Enhanced tetracycline adsorption using alginate-graphene-ZIF67 aerogel. *Colloids Surf., A* **2020**, *588*, 124360.

https://doi.org/10.1021/acsomega.1c03479
ACS Omega 2021, 6, 23528−23541

(55) Bhagyaraj, S.; Krupa, I. Alginate-mediated synthesis of hetero-shaped silver nanoparticles and their hydrogen peroxide sensing ability. *Molecules* **2020**, *25*, 435.
(56) Gholizadeh, B. S.; Buazar, F.; Hosseini, S. M.; Mousavi, S. M. Enhanced antibacterial activity, mechanical and physical properties of alginate/hydroxyapatite bionanocomposite film. *Int. J. Biol. Macromol.* **2018**, *116*, 786−792.
(57) Zhao, X. H.; Li, Q.; Ma, X. M.; Xiong, Z.; Quan, F. Y.; Xia, Y. Z. Alginate fibers embedded with silver nanoparticles as efficient catalysts for reduction of 4-nitrophenol. *RSC Adv.* **2015**, *5*, 49534−49540.
(58) Bahrami, A.; Kazeminezhad, I.; Abdi, Y. Pt-Ni/rGO counter electrode: electrocatalytic activity for dye-sensitized solar cell. *Superlattices Microstruct.* **2019**, *125*, 125−137.
(59) Yu, S.; Liu, J.; Zhu, W.; Hu, Z.-T.; Lim, T.-T.; Yan, X. Facile room-temperature synthesis of carboxylated graphene oxide-copper sulfide nanocomposite with high photodegradation and disinfection activities under solar light irradiation. *Sci. Rep.* **2015**, *5*, 16369.
(60) Wu, R.; Qian, X.; Zhou, K.; Liu, H.; Yadian, B.; Wei, J.; Zhu, H.; Huang, Y. Highly dispersed Au nanoparticles immobilized on Zr-based metal−organic frameworks as heterostructured catalyst for CO oxidation. *J. Mater. Chem. A* **2013**, *1*, 14294−14299.
(61) Luceño-Sánchez, J. A.; Díez-Pascual, A. M. Grafting of polypyrrole-3-carboxylic acid to the surface of hexamethylene diisocyanate-functionalized graphene oxide. *Nanomaterials* **2019**, *9*, 1095.
(62) Zheng, X.; Yu, H.; Yue, S.; Xing, R.; Zhang, Q.; Liu, Y.; Zhang, B. Functionalization of graphene and dielectric property relationships in PVDF/graphene nanosheets composites. *Int. J. Electrochem. Sci.* **2018**, *13*, 1−13.
(63) Parhi, P.; Ramanan, A.; Ray, A. R. Preparation and characterization of alginate and hydroxyapatite-based biocomposite. *J. Appl. Polym. Sci.* **2006**, *102*, 5162−5165.
(64) Iqbal, J.; Shah, N. S.; Sayed, M.; Imran, M.; Muhammad, N.; Howari, F. M.; Alkhoori, S. A.; Khan, J. A.; Khan, Z. U. H.; Bhatnagar, A.; Polychronopoulou, K.; Ismail, I.; Haija, M. A. Synergistic effects of activated carbon and nano-zerovalent copper on the performance of hydroxyapatite-alginate beads for the removal of As^{3+} from aqueous solution. *J. Cleaner Prod.* **2019**, *235*, 875−886.
(65) Cao, Y.; Zhao, Y.; Lv, Z.; Song, F.; Zhong, Q. Preparation and enhanced CO_2 adsorption capacity of UiO-66/graphene oxide composites. *J. Ind. Eng. Chem.* **2015**, *27*, 102−107.
(66) Saleem, A.; Wang, J.; Sun, T.; Sharaf, F.; Haris, M.; Lei, S. Enhanced and selective adsorption of Copper ions from acidic conditions by diethylenetriaminepentaacetic acid-chitosan sewage sludge composite. *J. Environ. Chem. Eng.* **2020**, *8*, 104430.
(67) Eltaweil, A. S.; El-Tawil, A. M.; Abd El-Monaem, E. M.; El-Subruiti, G. M. Zero Valent Iron Nanoparticle-Loaded Nanobentonite Intercalated Carboxymethyl Chitosan for Efficient Removal of Both Anionic and Cationic Dyes. *ACS Omega* **2021**, *6* (9), 6348−6360.
(68) Bentahar, S.; Dbik, A.; El Khomri, M.; El Messaoudi, N.; Lacherai, A. Adsorption of methylene blue, crystal violet and congo red from binary and ternary systems with natural clay: Kinetic, isotherm, and thermodynamic. *J. Environ. Chem. Eng.* **2017**, *5*, 5921−5932.
(69) Mouni, L.; Belkhiri, L.; Bollinger, J.-C.; Bouzaza, A.; Assadi, A.; Tirri, A.; Dahmoune, F.; Madani, K.; Remini, H. Removal of Methylene Blue from aqueous solutions by adsorption on Kaolin: Kinetic and equilibrium studies. *Appl. Clay Sci.* **2018**, *153*, 38−45.
(70) Seera, S. D. K.; Kundu, D.; Gami, P.; Naik, P. K.; Banerjee, T. Synthesis and characterization of xylan-gelatin cross-linked reusable hydrogel for the adsorption of methylene blue. *Carbohydr. Polym.* **2021**, *256*, 117520.
(71) He, Y.; Gou, S.; Zhou, L.; Tang, L.; Liu, T.; Liu, L.; Duan, M. Amidoxime-functionalized polyacrylamide-modified chitosan containing imidazoline groups for effective removal of Cu2+ and Ni2+. *Carbohydr. Polym.* **2021**, *252*, 117160.
(72) Mi, F.-L.; Wu, S.-J.; Lin, F.-M. Adsorption of copper(II) ions by a chitosan−oxalate complex biosorbent. *Int. J. Biol. Macromol.* **2015**, *72*, 136−144.
(73) Karami, S.; Zeynizadeh, B. Reduction of 4-nitrophenol by a disused adsorbent: EDA-functionalized magnetic cellulose nanocomposite after the removal of Cu2+. *Carbohydr. Polym.* **2019**, *211*, 298−307.
(74) Tao, E.; Ma, D.; Yang, S.; Hao, X. Graphene oxide-montmorillonite/sodium alginate aerogel beads for selective adsorption of methylene blue in wastewater. *J. Alloys Compd.* **2020**, *832*, 154833.
(75) Li, H.; Liu, L.; Cui, J.; Cui, J.; Wang, F.; Zhang, F. High-efficiency adsorption and regeneration of methylene blue and aniline onto activated carbon from waste edible fungus residue and its possible mechanism. *RSC Adv.* **2020**, *10*, 14262−14273.
(76) Jawad, A. H.; Abdulhameed, A. S. Mesoporous Iraqi red kaolin clay as an efficient adsorbent for methylene blue dye: adsorption kinetic, isotherm and mechanism study. *Surf.Interfaces* **2020**, *18*, 100422.
(77) Chen, S.; Shen, W.; Yu, F.; Hu, W.; Wang, H. Preparation of amidoximated bacterial cellulose and its adsorption mechanism for Cu^{2+} and Pb^{2+}. *J. Appl. Polym. Sci.* **2010**, *117*, 8−15.
(78) Zhao, L.-X.; Liang, J.-L.; Li, N.; Xiao, H.; Chen, L.-Z.; Zhao, R.-S. Kinetic, thermodynamic and isotherm investigations of Cu^{2+} and Zn^{2+} adsorption on Li-Al hydrotalcite-like compound. *Sci. Total Environ.* **2020**, *716*, 137120.
(79) Hosseinzadeh, H.; Ramin, S. Effective removal of copper from aqueous solutions by modified magnetic chitosan/graphene oxide nanocomposites. *Int. J. Biol. Macromol.* **2018**, *113*, 859−868.
(80) Eltaweil, A. S.; El-Monaem, E. M. A.; Mohy-Eldin, M. S.; Omer, A. M. Fabrication of attapulgite/magnetic aminated chitosan composite as efficient and reusable adsorbent for Cr (VI) ions. *Sci. Rep.* **2021**, *11* (1), 1−15.

https://doi.org/10.1021/acsomega.1c03479
ACS Omega 2021, 6, 23528−23541